Substituent effects in iron porphyrin catalysts for the hydrogen evolution reaction

Nils Heppe[a]§, Charlotte Gallenkamp[a],[b]§, Stephen Paul[a], Nicole Segura-Salas[a], Niklas von Rhein,[b] Bernhard Kaiser[c], Wolfram Jaegermann[c], Atefeh Jafari[d], Ilya Sergeev[d], Vera Krewald*[b] and Ulrike I. Kramm*[a]

[a] Catalysts and Electrocatalysts, Department of Inorganic Chemistry, Technical University Darmstadt, Otto-Berndt-Str. 3, 64287 Darmstadt (Germany); E-mail: ulrike.kramm@tu-darmstadt.de

[b] Department of Theoretical Chemistry, Technical University Darmstadt, Alarich-Weiss-Str. 4, 64287 Darmstadt (Germany); E-mail: vera.krewald@tu-darmstadt.de

[c] Institute of Materials Science, Surface Science Division, Technical University Darmstadt, Otto-Berndt-Str. 3, 64287 Darmstadt (Germany)

[d] Deutsches Elektronen-Synchrotron, Notkestraße 85, 22607 Hamburg (Germany)

§ contributed equally

Abstract: For a future hydrogen economy, non-precious metal catalysts for the water splitting reactions are needed that can be implemented on a global scale. MNC catalysts with MN_4 active sites show promising performance, but an optimization rooted in structure-property relationships has been hampered by their low structural definition. Porphyrin model complexes are studied to transfer insights from well-defined molecules to MNC systems. This work combines experiment and theory to evaluate the influence of porphin substituents on the electronic and electrocatalytic properties of MN_4 centers with respect to the hydrogen evolution reaction (HER) in aqueous electrolyte. We found that the choice of substituent affects their utilization on the carbon support and their electrocatalytic performance. We propose an HER mechanism for supported iron porphyrin complexes involving a $[Fe^{II}(P^{\bullet})]^{-}$ radical anion intermediate, in which a porphinic nitrogen atom acts as an internal base. While this work focuses on the HER, the limited influence of a simultaneous interaction with the support and an aqueous electrolyte will likely be transferrable to other catalytic applications.

Introduction

To halt the global temperature increase, drastic transitions in energy production and storage are required. During the last decade, the global electricity production by renewable energy duplicated and is predicted to keep growing rapidly.[1] However, a major problem for the large scale implementation of renewable energies is the mismatch between production and demand. Compensating this discrepancy requires matching buffer capacities. The key principle for a hydrogen fueled society is to facilitate hydrogen (H_2) as a storable energy carrier. In this scenario, excess energy is used in water electrolysis to produce hydrogen. Alternatively, a direct conversion of solar energy to hydrogen in a photo-electrochemical cell (PEC) promises higher overall efficiency by utilizing synergetic effects of photoabsorption and water splitting,[2] so that the system can be operated in a decentralized way. In such systems, photoabsorbers can generate the required photovoltage, while catalysts decrease the overpotential of the oxygen and hydrogen evolution reaction (OER, HER) for overall water splitting.[3]

The maximum photon flux from solar irradiation limits the current density to 10 mA cm^{-2} on a flat substrate with an electrode area equal to its photoabsorber size.[2,4] For low current densities, cheap and earth abundant metal-nitrogen-carbon (MNC; M = Mn, Fe, Co, Ni, Mo) catalysts hold promise to replace platinum-type catalysts for the hydrogen evolution reaction (HER).[5] MNC catalysts are better known for their excellent activity in the oxygen reduction reaction (ORR).[6] They are also attractive for the CO_2 reduction reaction (CO_2RR) yielding valuable green fuels or base chemicals.[5c,7] One notable property of these materials is that the selectivity of the reduction process can be manipulated by varying the nature of the metal center or its chemical environment.[5b,7c,8]

Almost all MNC catalysts are prepared via a high temperature pyrolysis which results in a material with varying degrees of structural disorder. The low definition and the presence of side phases hinders systematic investigations.[9] This impedes the development of structure-property-relationships and consequently a knowledge-based optimization of the preparation process towards optimal catalyst activity. Intensive structural characterization has shown the active center in MNC catalysts to be constituted of single metal atoms incorporated into an amorphous carbon structure by coordination of N donor atoms, which are covalently doped into the carbon layers, see Figure 1a for a schematic depiction. The configuration of the N atoms surrounding the metal center and the geometry of the ligand sphere are still under debate,[6c,9b,10] but most suggestions for the active site structure have a square planar nitrogen coordination environment in common.[11]

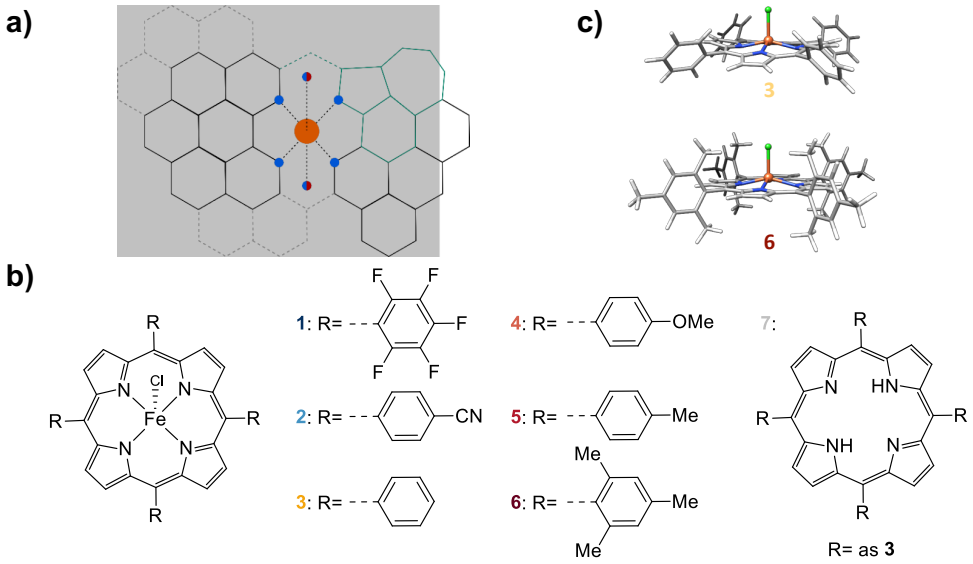

Figure 1: a) Structural motif of an Fe-N-C catalyst, **b)** the complexes studied herein with the substituents R = (**1**) $TPP(F)_{20}$-FeCl, (**2**) $TPP(CN)_4$-FeCl, (**3**) TPP-FeCl, (**4**) $TPP(OMe)_4$-FeCl, (**5**) $TPP(Me)_4$-FeCl, (**6**) $TPP(Me)_{12}$-FeCl and (**7**) TPP-H_2, **c)** three-dimensional side view of the geometry optimized by DFT exemplarily shown for complexes **3** and **6**.

Porphyrins have discrete MN_4 architectures that render them popular precursors for MNC catalyst preparation and spectroscopic models,[12] in particular to better understand the influence of porphyrin substituents on the M-N bonding character and resulting properties. The rich literature on porphyrins contains many examples that describe the effect of such chemical variations, for instance on the redox potentials,[13] or the influence on the reactivity of the complex.[14]

Most processes catalysed by porphyrin metal complexes take place in the M-X axial binding sites.[15] For the HER, substitution effects in homogeneous catalysis have been reported, e.g. by incorporating internal acids in the vicinity of the axial binding sites.[16] In contrast to HER on platinum, where the HER mechanism is thought to proceed via consecutive proton-coupled electron transfer (PCET) steps, HER on iron porphyrins involves two initial reduction steps of the Fe(III) center to Fe(I) with subsequent oxidative protonation of the active site.[16a,16c]

To the best of our knowledge, no systematic study of substitution effects on metal porphyrins in a heterogeneous system for the HER exists to date. This represents a significant gap in knowledge because the simultaneous interaction of porphyrins with the aqueous electrolyte and with a carbon support may influence the hydrogen evolution reactivity significantly.[17] This study makes a contribution towards closing this gap by building a bridge between homogeneous catalysis and three dimensional systems such as MNC catalysts. Focusing on Fe-porphyrins, we investigate the influence of substituents and the effect that the immobilization on a high-surface area carbon support has on the redox characteristics, spectroscopic properties and electrocatalytic HER behaviour. The catalytic activity is correlated with structural characteristics extracted from X-ray photoelectron spectroscopy (XPS) and nuclear resonance vibrational spectroscopy (NRVS). Additionally, density functional theory (DFT) calculations on all iron porphyrin complexes complement the experimental findings and shed light on the HER mechanism in supported porphyrin complexes.

Results and Discussion

For this systematic study of substituent effects on the properties and catalytic activity of iron porphyrin complexes, six variants of the phenyl rings in the parent complex [Fe(TPP)Cl], TPP: tetraphenylporphyrin, were chosen. The phenyl substituents are expected to increase the electron density at the FeN_4 center from **1** to **6**, see Figure 1b. For **1** and **2**, a mesomeric or inductive electron withdrawing effect is expected, whereas the substituents of **4**-**6** are electron donating. Since inductive effects are considered rather weak, substitution patterns with multiple groups were chosen for **1** and **6**. To assess the importance of rotational degrees of freedom of the phenyl group relative to the porphyrin ring, porphyrin **5** is used as an additional example for electron donation via an inductive effect. The parent complex **3** serves as a reference substance, and the free porphyrin **7** as a reference for activity measurements to confirm that the observed catalytic activity stems from the metal center as the active site (see section 'mechanistic insights' below).

The substituents influence the orientation of the phenyl ring relative to the porphyrin plane, as is exemplarily shown in Figure 1c for complexes **3** and **6**. This tilt affects the conjugation between the phenyl π-electrons and the π-electrons of the porphyrin ring (SI-Figure-S4 and S5) and hence the properties of the complexes. Furthermore, it can be reasonably expected that this aspect of the structure can alter the porphyrin-support interface: it affects the distance between the metal center and the underlying graphene plane, the adsorption of the porphyrin on the carbon support, their electronic interaction or a partial rotation/distortion of the substituents. Vice versa, the degree of interaction with the support may result in altered electronic properties or stabilities of the complexes.

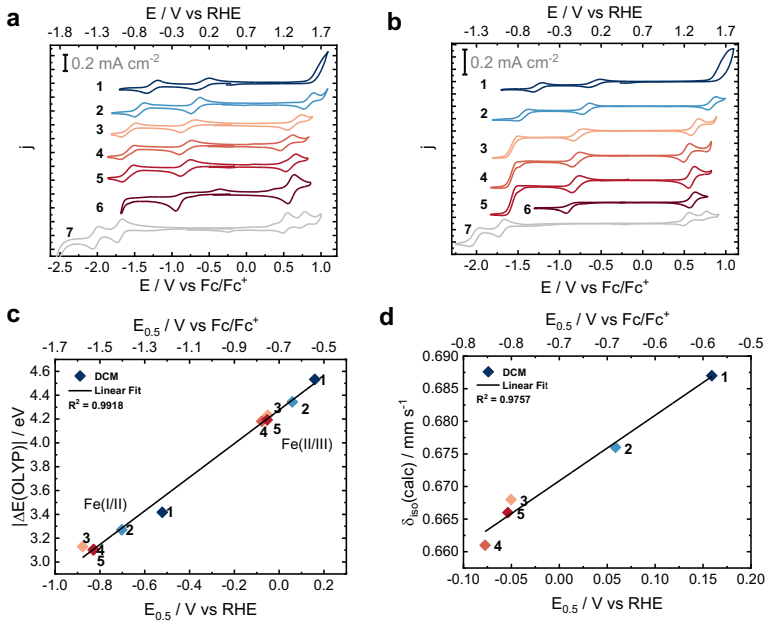

Figure 2: Cyclic voltammograms of 1 mM Fe(III)-porphyrin and 0.1 M TBAP in DCM with a scan rate of **a**) 100 mV s^{-1} and **b**) 10 mV s^{-1}. Correlation between redox potentials of Fe(II/III) and Fe(I/II) with **c**) electronic energy differences from DFT calculations with the OLYP density functional and **d**) isomer shift values of the Fe(II) species computed with the B3LYP density functional.

Redox properties in organic solvent. To determine the redox properties of the porphyrins without any support effects, a first set of measurements was conducted in organic solvent. Because of the large potential range accessible, dichloromethane (DCM) with tetrabutylammonium perchlorate (TBAP) as a conductive agent was chosen as the electrolyte. Figure 2a and b show the cyclic voltammograms (CVs) of **1**-**7** at 100 mV s^{-1} and 10 mV s^{-1}, respectively.

Three main redox events can be distinguished. Depending on the substituent, the first feature around 1.2 to 1.7 V *vs* RHE corresponds to the redox event in the porphyrin π-system.[18] This transition appears stable and reversible for all porphyrin complexes except for **1** where an irreversible decomposition takes place. The strong electron withdrawing effect of the fluoro substituents suggests that their presence destabilizes a higher oxidation state of either the iron center (i.e. Fe^{IV}) or the delocalized π-system.

The second redox feature around 0.3 and -0.3 V *vs* RHE corresponds to the Fe^{II}/Fe^{III} redox transition. Consequently, no redox event is found in reference material **7**. The Fe(II/III) redox potentials for **1**,[14] **3**,[14,19] **4**,[14] **5**[14] and **6**[20] determined here are in good agreement with literature data. To the best of our knowledge there is no suitable reference data with comparable choices of solvent and conducting agent available for **2**.

The separation between anodic and cathodic peak and their similar intensities indicate that the Fe^{II}/Fe^{III} redox transition is a reversible transition for all iron porphyrin complexes except for **6**. The highly electron donating effect of the mesityl groups in **6** may destabilize the reduced state, which can be understood as a highly reactive Fe^{II} species. Since after the reduction peak, no anodic peak appears in the reverse direction, the follow-up reaction has to be of non-electrochemical nature. This is also indicated by the small oxidation peak at ~0.35 V vs RHE which only appears in the anodic sweep at 100 mV s^{-1}, but is absent at 10 mV s^{-1} of **6**. This peak is likely not associated with the oxidation back to the intact Fe^{III} porphyrin. Instead we suggest that the cathodic sweep at U < -0.3 V *vs* RHE produces an unspecified intermediate from **6**, the decay products of which can be oxidized at high sweep rates.

The third main redox event in the potential range of -0.3 to -1.0 V *vs* RHE is assigned to the transition between Fe^{II} and Fe^{I}. For the Fe(I/II) redox potentials determined here, reference data is only available for **3**[19] and **6**,[20] which is in good agreement. For **1** and **2,** the transition is reversible, whereas **3** to **5** show a distorted pair of redox peaks at 100 mV s^{-1} and a narrow step at 10 mV s^{-1}. The latter can be interpreted as a synproportionation of Fe^{I} generated on the electrode and Fe^{III} from solution to Fe^{II} which also explains the lack of a reoxidation peak on the back sweep.[16a] This observation indicates a higher reactivity at reduced states when the substitution pattern induces a higher electron density at the iron center.

We note that the assignment of Fe^{I} as a formal oxidation state should be treated with caution. The electronic structure may be formulated in terms of either the formal oxidation state $[Fe^{I}(P)]^{-}$ or the physical or spectroscopic oxidation state $[Fe^{II}(P^{\bullet})]^{-}$.[21] Both resonance structures have been assigned from spectroscopic experiments,[22] and their formation is heavily dependent on the substitution pattern.[22,23] The electronic structures obtained from density functional theory (DFT) calculations show π-radical anion character throughout the series. In all species, the spin delocalized over the porphyrin ring is antiparallel to the unpaired electrons on the iron ion, in line with previous reports of this type of electronic structure.[23b] Nevertheless, this reduced state will be referred to both as Fe^{I} and $[Fe^{II}(P^{\bullet})]^{-}$ in the following.

The reduction potentials of the free base porphyrin **7** show that the formation of the free radical cation lies just a few mV below the half wave potentials ($E_{0.5}$) of the discussed Fe^{I}/Fe^{II} transition. The observed trends indicate that the radical anion character is more pronounced the lower the $E_{0.5}$ of the $[Fe^{II}(P^{\bullet})]^{-}/Fe^{II}$ couple

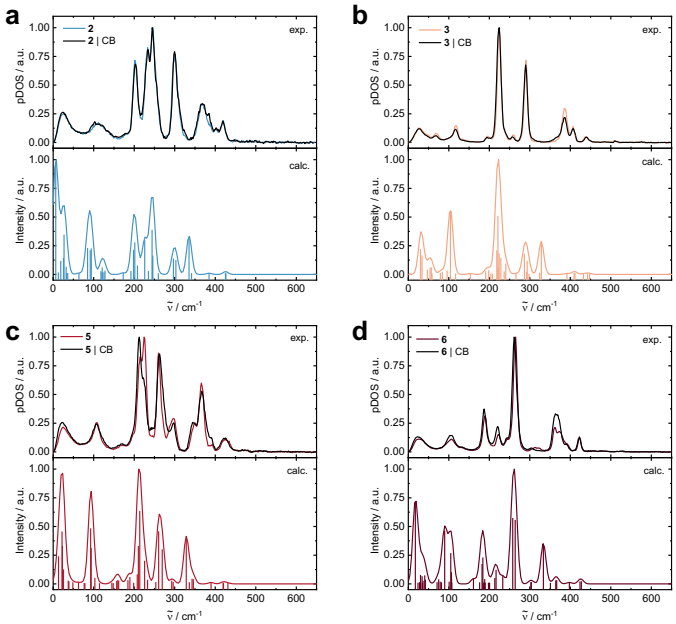

Figure 3: ^{57}Fe-pDOS derived from NRVS measurements (exp.) of **a) 2**, **b) 3**, **c) 5** and **d) 6** between 17 and 28 K. Compared are as-prepared porphyrins and their carbon-supported counterparts labeled "| CB" as well as predicted NRV spectra from DFT (calc.).

and hence the tendency for synproportionation with Fe^{III} porphyrin from solution is.

The experimental redox potentials (100 mV s^{-1}) are compared against the electronic energy differences from DFT single point calculations of the reduced and oxidized species using the OLYP density functional. This straightforward approach does not consider a reference redox couple and thus cannot yield absolute redox potentials. Nevertheless, it has been applied successfully in the past and is therefore used in this work.[24] The resulting energy differences, reported in eV, correlate extremely well with the redox potentials obtained experimentally in organic solvent (linear regression with $R^2 > 0.99$, see Figure 2c). Consequently, the computational approach chosen here could be employed as a calibration for future predictions of redox events in similar catalyst models.

Since the isomer shift from Mössbauer spectroscopy is inversely proportional to the electron density at the nucleus, it can serve as a further measure of the electron density in the series.[25] Figure 2d shows that the predicted isomer shift values of the Fe^{II} species correlate well with the experimentally determined half wave potentials of the Fe^{II}/Fe^{III} couple in organic solvent.[26] The iron porphyrin complexes with electron donating substituents have a lower isomer shift and therefore a higher electron density at the iron center than the iron porphyrins with electron withdrawing groups. These results confirm the expected trend and furthermore establish a direct correlation between the half wave potentials and the electron density at the FeN_4 moiety. It is thus possible to link the predicted electronic structures and electron densities to the measured redox potentials via a spectroscopic property.

Note that no experimental $E_{0.5}$ was determined for **6** due to the irreversibility of Fe(III) reduction and therefore this data point is absent in Figures 2c and d. From the predicted value of the electronic energy difference, 4.23 eV, an $E_{0.5}$ data point at -0.03 V *vs* RHE for Fe^{II}/Fe^{III} can be predicted. For the same redox event, the Fe(II) isomer shift at 0.678 mm s^{-1} would correspond to an $E_{0.5}$ data point at 0.07 V *vs* RHE. For the $[Fe^{II}(P^{\bullet})]^{-}/Fe^{II}$ transition, the computed electronic energy difference is 3.02 eV which would correspond to -0.887 V *vs* RHE in the experiment.

Table 2: Assignment and energetic position of vibrational modes for NRV spectra of **2**, **3**, **5** and **6** and the frequencies predicted by DFT. Frequencies are given in cm^{-1}.

	2		**3**		**5**		6	
	Frequency (cm^{-1})							
	exp.	calc.	exp.	calc.	exp.	calc.	exp.	calc.
γ_9 (doming)	112	94, 121	117	104	107	93, 94	106	90
Fe-Cl stretch	366	335	387	329	366	328, 336	363, 373	334
υ_{50}	420	425, 426	407	409, 412	426	420, 420	422	424, 427
γ_6 (inverse doming)		208, 260		237, 266		199, 233, 253		161, 233
υ_8 (breathing)		385		392		390		398

Support effects detected by nuclear resonance vibrational spectroscopy. To better understand the transferability of the results from homogeneous electrochemistry in organic solvent to heterogeneous electrochemistry of the carbon-supported porphyrins in aqueous electrolyte, nuclear resonance vibrational spectroscopy (NRVS) was performed on selected ^{57}Fe-enriched porphyrins (**2**, **3**, **5** and **6**) with and without carbon support. NRVS selectively probes the vibrational modes involving iron and has been used to characterize heme-type complexes and FeNC materials.[9c,27]

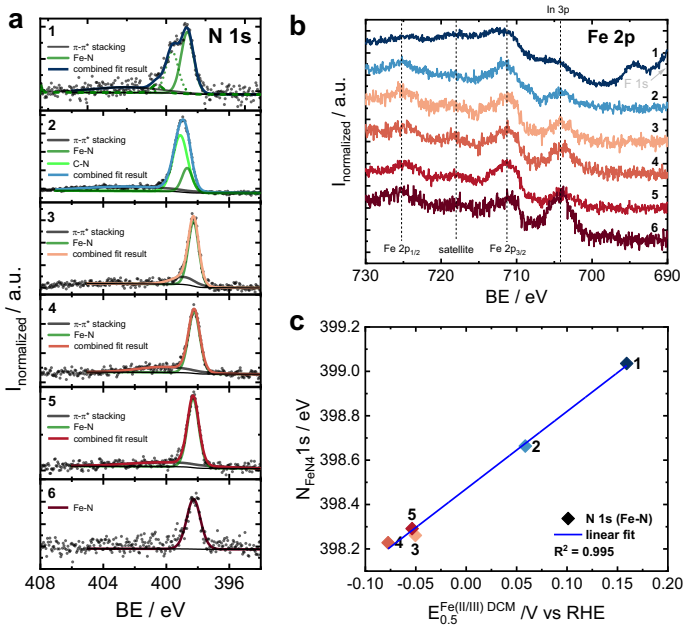

Figure 4: XPS results of porphyrins **1** - **6** impregnated on CB; HR-XPS of the **a)** N1s region; **b)** Fe2p region; **c)** correlation between the binding energy associated with the FeN_4 peak and the redox potential $E_{0.5}$ of Fe(II/III) in DCM.

NRV spectra can generally be divided into three main ranges: (i) below 200 cm^{-1}, there are mostly out-of-plane modes and the doming mode, (ii) between 200 - 400 cm^{-1}, most modes have in-plane character, (iii) between 400 - 600 cm^{-1}, modes typically involving the axial ligand are found.[27a] Below 50 cm^{-1}, phonon modes resulting from translation of the molecule in the solid are found; since these cannot be predicted by DFT calculations of a single molecule, they will not be discussed below.

For heme-type molecules, the highly symmetric (D_{4h}) iron porphin Fe(P) core serves as a reference compound for assigning and discussing the most important vibrational modes.[27a,27c,28] A_1 symmetric out-of-plane motions of iron such as the doming mode (γ_9) or the inverse doming modes (γ_6, γ_7) are thought to influence reactivity in axial direction.[27c,28a,28b] The stretching mode of the Fe-L bond, where L denotes the axial ligand, gives further information on the bond strength. In-plane modes of *E* symmetry stretching the Fe-N bonds are referred to as υ_{50} and υ_{53}, and result in dominating features due to the high relative motion of Fe within these modes and are located at 407 to 426 cm^{-1}.[27c] From the work of Barabanschikov *et al.* on how the NRVS changed from unsubstituted Fe(P)Cl to substituted Fe(OEP)Cl and Fe(PPIX)Cl, it is known that asymmetric substitutions can have a strong impact on modes that influence ligand binding and dissociation.[27c] For aryl substituted Fe(P), namely the Fe(TPP) family, various NRVS studies for different axial ligands and aryl substitution patterns were performed.[28,29] These studies found that vibrational modes of biorelevant axial ligands such as O_2, NO, CO or imidazole derivatives couple with those of the rest of the molecule.[28] The distortion of the aryl rings was found to couple strongly with in-plane modes, so that υ_{50} and υ_{53} split into several signals.[28b] For the aryl substituents of Fe(P)Cl (C_{4v} symmetry), it is usually assumed that the symmetry of the molecule does not change which would allow an easier assignment of the modes.[30] However, the aryl rings are not likely to be oriented perpendicular to the porphin plane, but at a smaller angle, thus lifting the symmetry and hence the degeneracy of *E* symmetric vibrations.

The NRV spectra of **2**, **3**, **5** and **6** are shown in Figure 3; the experimental vibrational frequencies are given in SI-Table S11, and the predicted vibrational frequencies and modes are described in SI-Table S12. By comparison to the NRVS of Fe(P)Cl and the predicted DFT spectra, the doming mode γ_9, the inverse doming mode γ_6, the Fe-Cl stretch and two in-plane vibrations υ_{50} can be assigned (see Table 2).

The signals in the NRV spectrum of complex **3** are consistent with spectra for similar complexes with different axial ligands,[28] and the Fe-Cl stretch fits previous Raman spectroscopy data.[30] Moreover, the experimental and calculated pDOS of all four complexes are in excellent agreement except for the vibrations involving the chlorine ligand, which are underestimated as has been seen previously in the literature.[27c,30] A clear effect of the aryl ring substituents on the Fe-Cl stretch is not observed.

The doming modes γ_9 are sensitive to the substitution pattern, although the influence of electronic effects and differing molecular weights cannot be discerned (exp: 112 cm^{-1}, 117 cm^{-1}, 107 cm^{-1}, and 106 cm^{-1} for **2**, **3**, **5**, and **6**). This shift is also observed for predicted positions of the inverse doming mode γ_6 which cannot be clearly assigned in the experiment due to overlay with more intense in-plane vibrations. The less intense in-plane modes show a shift to higher frequency for υ_{50} or no significant change for υ_8 (breathing mode).

A general substituent effect for the more intense in-plane Fe-N stretching modes is more difficult to state. Substitution in *para* position of the aryl rings has a similar effect for **2** and **5**. The bending (and rotation) motions of the -CN or $-CH_3$ substituents are coupled to the in-plane Fe-N stretching modes, which likely further lifts the degeneracy of these vibrations. In contrast to that, **6** shows a larger number of degenerate Fe-N stretching vibrations and fewer, but more well-defined modes. As the aryl rings have methyl substituents in both *ortho* positions, steric effects enforce an almost perpendicular orientation to the porphin plane, which brings **6** closer to C_{4v} symmetry than its analogues in which the aryl rings are rotated. Another observation is that for **6**, the modes

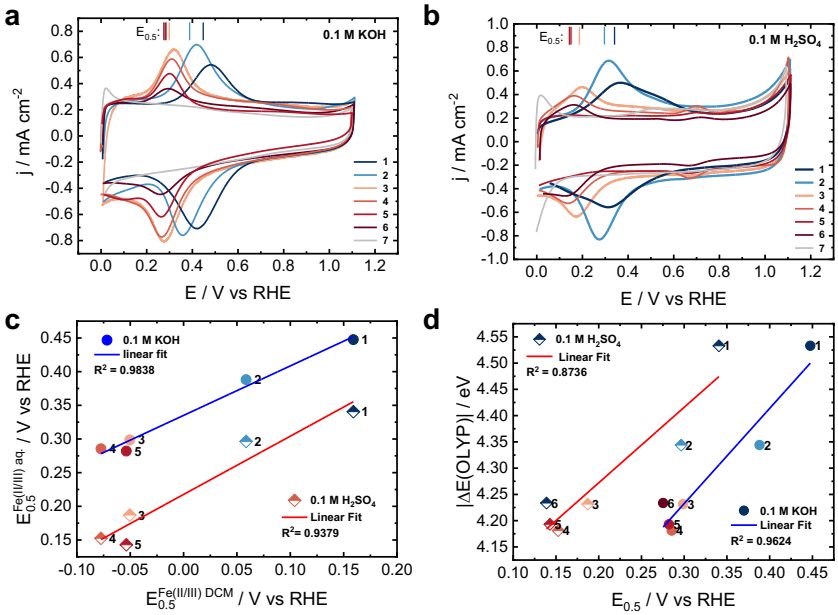

Figure 5: Cyclic voltammograms of carbon-supported Fe(III)-porphyrins **a**) in KOH of pH = 13 and **b**) in H_2SO_4 of pH = 1 where the vertical lines above the CVs indicate the position of Fe(II/III) half wave potentials $E_{0.5}$; all measurements performed with an electrode loading of 0.5 mg_{cat} cm^{-2}. **c**) Correlation between $E_{0.5}$ of Fe(II/III) at pH = 13 and pH = 1 *vs* the corresponding $E_{0.5}$ of Fe(II/III) values in DCM. **d**) Correlation between electronic energy differences from OLYP single point calculations and $E_{0.5}$ of Fe(II/III) at pH = 13 and pH = 1.

around 200 cm^{-1} are less intense than in **2**, **3** and **5**; this is because the aryl motion dominates these modes rather than the iron motion.

The experimental data show no (**2**, **3**) or at most a minor (**5**, **6**) effect of the carbon support on the positions and intensities of the vibrational modes. It can thus be concluded that the carbon support interacts only weakly with the systems investigated here. This is further corroborated by the excellent agreement between experiment and calculation, and hence the use of a molecular model appears fully justified to analyze the spectroscopic, electrochemical and catalytic data presented in the following.

Structural investigation by XPS. The near-surface composition was investigated by X-ray photoelectron spectroscopy (XPS). The results for the characteristic N 1s and Fe 2p signals can be found in Figures 4a and b, the survey spectra are shown in Figure S1. The impregnated model catalysts were investigated as powders by pressing them onto an indium foil as the sample carrier (see experimental details for more information). In consequence, the In 3p signal (~704 eV) occurs in all Fe 2p spectra in varying intensities depending on the quality of the catalyst layer on In.

It is well known that the energetic position of the N 1s peak related to metal-nitrogen coordination is quite sensitive to the electronic state of the coordinating iron ion.[31] Besides the main Fe-N_4 peak, a second peak arises at higher binding energy values and is attributed to the same origin, but broadened by π-stacking. The Fe-N_4 signal of **1** shows a further broadening which could indicate the presence of a further signature. With this assumption, it was deconvoluted into two narrow main signals and a minor signal. The additional species is assumed to be a side product of the purchased iron porphyrin, i.e. with varying fluorine bonds on the phenyl substituents (see also the XP spectra for the as-received porphyrin **1** SI-Figure S2).

Once more, a correlation between the spectroscopic results and the electrochemical characteristics can be observed. Figure 4c shows a good correlation between increasing binding energy of the related N 1s peak and increasing redox potential (linear regression with $R^2 > 0.99$; note: the value for **1** is averaged for the two main Fe-N_4 components; **6** is again not included due to irreversibility of Fe(III) reduction in DCM). The calculated N 1s orbital energies for the chlorides **1 – 6** also fit well to the binding energies obtained from XPS (see SI-Figure S8).

Redox properties of the supported porphyrins in aqueous solvent. Having clarified the structural characteristics and shown that there is only a minor influence of the carbon support, the CVs of the carbon supported systems in alkaline and acidic electrolyte were measured, see Figures 5a and b. The measurements were performed in a much smaller potential range of 0.0 to 1.1 V vs RHE (compare -1.8 to 1.7 V vs Fc in DCM) defined by the stability window of the aqueous electrolyte. Therefore, only one redox transition can be identified and assigned to Fe^{II}/Fe^{III}.[15b,32] The general trend observed in aqueous electrolyte is the same as in organic electrolyte: electron withdrawing groups shift the $E_{0.5}$ values to higher potentials while electron donating substituents shift the potentials to lower potentials (see Table 1 for the exact redox potential values).

The $E_{0.5}$ determined in both aqueous electrolytes correlate well with the values obtained from the measurements in DCM, see Figure 5c. The slope of the regression line deviates from 1, indicative of a solvent or support effect on the redox behavior. While identifying the dominant effect is beyond the scope of this work, it is noted that a more pronounced deviation of the potentials is seen in the acidic vs. organic media. A plausible explanation may lie in a stronger interaction of the material with the acidic environment: substituents with free electron pairs (**2**

and **4**) may be (partially) protonated, which could bias the comparison, and similarly a (partial) protonation of the CB surface is expected to affect the porphyrin-support interface.
We note that the energy differences predicted by DFT correlate better with $E_{0.5}$ in alkaline than for acidic electrolyte (see Figure 5d), but are overall best correlated with the half wave potentials in organic electrolyte. It is likely that the simplified description of the redox events (no explicit solvent-solute interactions, no counter ion effects) reaches its limits here.
In the following, we will focus on the data obtained in 0.1 M KOH (see Figure S3b for acidic conditions with significantly lower HER activity). In the CVs in KOH (Fig. 5a), it can be noted that the peak shape and area of the redox signals varies depending on the porphyrin. All systems are compared in terms of the electrochemically active amount of iron on the electrode which can be calculated by integrating the peak area of the oxidation signal. The reduction peak was not considered as in most cases the baselines were less well defined leading to larger errors. SI-Figure S3 shows exemplarily for **4** how the charge q_a was determined, which is used in Equation 6 to determine the electrochemically active amount of Fe on the electrode $n_{Fe\text{-}EC}$

$$n_{Fe\text{-}EC} = \frac{q_a}{\upsilon F} \qquad (6)$$

with the scan rate υ and the Faraday constant F. It is assumed that each electrochemically active FeN_4 center contributes with a full electron transfer to the redox peak and the individual FeN_4 centers do not affect each other. The values of $n_{Fe\text{-}EC}$ were then compared to the stoichiometrically calculated amount expected on the electrode (n_{theo}) based on catalyst loadings. In Figure 6a, the electrochemically active amount of iron and the theoretically possible value are compared.
The electrochemically active iron, $n_{Fe\text{-}EC}$, amounts to only a fraction of the theoretical amount n_{theo}, see Figure 6a. The ratio of both values is the electrochemical utilization of iron, see Figure 6b where this quantity is plotted against the half wave potential of the Fe^{II}/Fe^{III} couple. This illustrates that the quality of the porphyrin-support interaction is influenced by the substituent induced chemical changes of the porphyrin structure. The utilization of iron ranges from 6-28% across the porphyrin series. The interaction with the carbon support is most favorable for electron poor FeN_4 porphyrins, while a high electron density leads to a weaker interaction with the support. Clearly, steric and electronic effects will play a role here. The former is especially important for ortho-substituted porphyrins **1** and **6**, where the phenyl groups are almost perpendicular to the porphyrin plane (see Table SI2, and Figure SI6). The latter may take the form of polarizability effects in the highly fluorinated **1**, where smaller van der Waals forces would be expected.

Mechanistic insights. The activity measurements of the iron porphyrin complexes towards water splitting in alkaline media are shown in Figure 7a. From the absolute value in the cathodic sweep, no direct trend can be derived. The drastic variations of the amount of electrochemically contacted iron on the electrodes are considered by calculating the turnover frequency (TOF, equation 7):

$$TOF = \frac{j\, A_{disk}}{n_{Fe\text{-}EC}\, F\, f} \qquad (7)$$

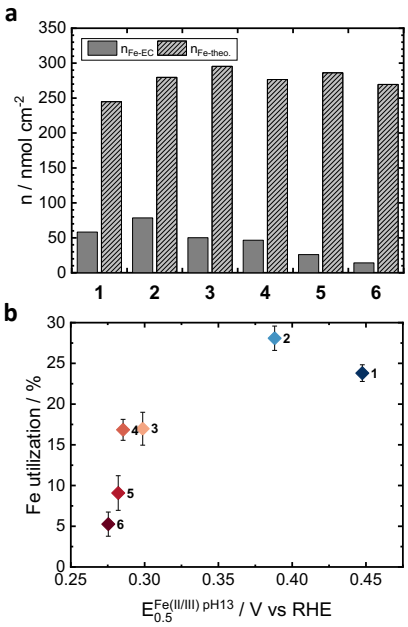

Figure 6: a) Theoretically expected iron amount on the electrode vs. electrochemically determined amount, **b)** Fe utilization (percentage of electrochemically contacted iron = $n_{Fe\text{-}EC}\, n_{theo}^{-1}$) over the Fe(II/III) redox potential.

From the product of the current density and the geometric electrode area A_{Disk}, the current is determined and then divided by $n_{Fe\text{-}EC}$, Faraday constant F and the stoichiometric factor *f* derived from the reaction equation of hydrogen formation. Figure 7b shows the turnover frequency (TOF) at an overpotential of 0.7 V and 0.8 V plotted against the $E_{0.5}$ Fe^{II}/Fe^{III}.
The results show a direct structure-property-relationship between the porphyrin substituents and their redox potentials as well as their HER activities: as the electron donating effect of the substituent increases, the redox potential of the Fe^{II}/Fe^{III} transition decreases and the TOF increases. To translate this relationship into systematic improvements of HER catalysts, a detailed understanding of the reaction mechanism is essential. However, investigations of metal porphyrins and specifically iron in neutral or alkaline electrolyte are rare and contain limited information on the reaction mechanism.[33] Beyene *et al.* extensively investigated the homogeneous HER of $TPP(SO_3H)_4$-Co^{II} among other cobalt and copper porphyrin complexes.[16b,34] They concluded that water acts as a proton source like a weak Brønsted acid for the oxidative protonation of the $[Co^0N_4]^{2-}$ species.
In analogy to this reaction mechanism for Co porphyrins, the following reaction steps were derived for iron porphyrins in organic solvents, i.e. homogeneous catalysts. After loss of the chloride ligand (equation 1), the hydrogen evolution reaction at metal porphyrin catalysts is initiated by a two electron reduction of the metal center (equations 2, 3).[16c,35] Subsequently, the intermediate $[M^{(n-2)}]$ undergoes an oxidative protonation yielding a metal hydride $[M^n\text{-H}]$ (equation 4). In organic electrolyte, a homolysis of two $[M^n\text{-H}]$ is also possible.[16d] The hydricity of metal hydrides was suggested as a descriptor for their HER activity.[36] In aqueous electrolyte, metal hydrides are not expected to be stable, so that a rapid protonation is likely (equation 5). Furthermore, the combination of two hydrides appears very unlikely for supported systems. It is therefore assumed that the

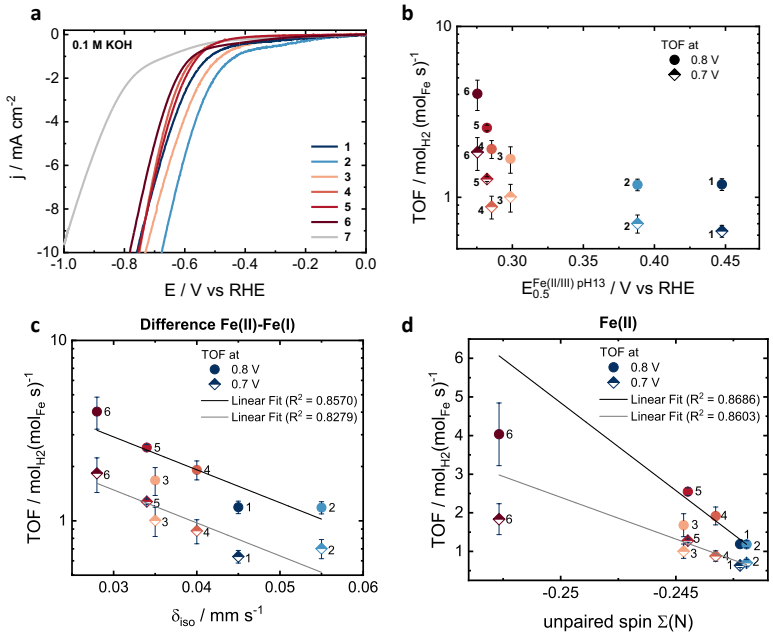

Figure 7: a) LSV in 0.1M KOH to determine the HER activity at pH13; correlation attempts between TOF and **b)** $E_{0.5}$ Fe(II/III); **c)** difference in δ_{iso} obtained for Fe(II)P and Fe(I)P (in spectroscopic oxidation state notation: $[Fe(II)(P^{\bullet-})]^-$); and **d)** sum of Mulliken spin populations on porphinic N in the Fe(II) complexes.

reaction proceeds via two reduction steps followed by two consecutive protonation steps at the same site.

Removal of chloride ligand[1]:	Fe(III)-Cl → Fe(III) + Cl^-	(1)
1st Reduction step:	Fe(III) + e^- → Fe(II)	(2)
2nd Reduction step:	Fe(II) + e^- → Fe(I)	(3)
Oxidative protonation	Fe(I) + H^+ → Fe(III)-H	(4)
Hydride protonation and H_2 release	Fe(III)-H + H^+ → Fe(III) + H_2	(5)

The mechanism is thought to be heavily dependent on the porphyrin complex, the electrolyte and the proton source. It was suggested that the formation of an M^{n-2} species Fe^I (or $[Fe^{II}(P^{\bullet})]^-$) respectively by two consecutive reduction steps (equation 2 and 3) is rate determining for porphyrin complexes in organic electrolyte, i.e. as a homogeneous catalyst.[16a,35]

This assumption seems to be invalid for the supported iron porphyrins in this study. Porphyrin **1** has the lowest overpotential towards $[Fe^{II}(P^{\bullet})]^-$ formation in DCM, but overall lowest TOF (at 0.7 V) in 0.1 M KOH. Further, complex **3** with the highest $[Fe^{II}(P^{\bullet})]^-$ overpotential only shows mediocre TOF. This leads to the conclusion that $[Fe^{II}(P^{\bullet})]^-/Fe^{II}$ potentials determined in organic electrolyte cannot be translated to HER activities in alkaline electrolyte. A possible explanation is that the stability of the doubly reduced $[Fe^{II}(P^{\bullet})]^-$ state with π-radical-anion character, which is documented in spectroscopic investigations of similar systems, differs in different media.[22,23c] This suggests that the $[Fe^{II}(P^{\bullet})]^-/Fe^{II}$ transition mostly depends on the ability of the π-system to stabilize the radical anion, making it a ligand centered transition in contrast to the metal centered Fe^{II}/Fe^{III} transition. The stability of the radical anion is not only influenced by the substituents but also by the solvent. For this reason, a comparison of the $[Fe^{II}(P^{\bullet})]^-/Fe^{II}$ potential determined in DCM and the HER activity in 0.1 M KOH is not reported in this study.

From the experimental results, a structure-property-relationship can be drawn: electron donating effects cause an increase in HER reactivity, presumably by destabilizing the Fe^{II} species. However, this effect seems to be not of pure electronic nature as the calculated isomer shift, a direct measure for the electron density at the Fe^{II} ion, does not correlate with the TOF, nor do the number of unpaired electrons and the charge at the iron ion (see SI Figure S12). The solvent interactions discussed above are thus not systematic throughout the series which would suggest water or hydroxide involved in the HER mechanism and in the rate determining step.

DFT calculations were performed to obtain further insights into the mechanism. The calculated Gibbs free enthalpies of all reaction steps for the mechanism expected in organic electrolyte (**A**, **B**, **C**, **E**, **J**) are shown in Figure 8. The Gibbs free enthalpies of each reaction step for each complex are plotted *vs* the TOF in the SI Figure S11. The abstraction of the chlorine ligand (**A**→**B** in Figure 8b) shows a good correlation; however, this reaction step is thought to take place in the beginning of the catalytic cycle.

The first reduction step Fe^{II}/Fe^{III} (**B**→**C**) shows the same behavior as the experimentally obtained redox potentials. The second reduction step $[Fe^{II}(P^{\bullet})]^-/Fe^{II}$ (**C**→**E**) and the further reaction from $[Fe^{II}(P^{\bullet})]^-$ to the hydride Fe^{III}-H (**E**→**J**) both show linear trends, but with relatively poor R^2 values. Note that the comparison of TOF with the Gibbs enthalpy as a purely thermodynamic property is only meaningful for small reaction barriers; transition states are required to link directly to kinetic information from experiments.

In further attempts to identify species involved in the rate-determining step, we investigated properties related to the electron densities of Fe^{II} and $[Fe^{II}(P^{\bullet})]^-$ (**E**, formally Fe(I)), since

[1] For the sake of simplicity, the porphyrin ligand and the total charge of the systems are not stated explicitly in the reaction equations.

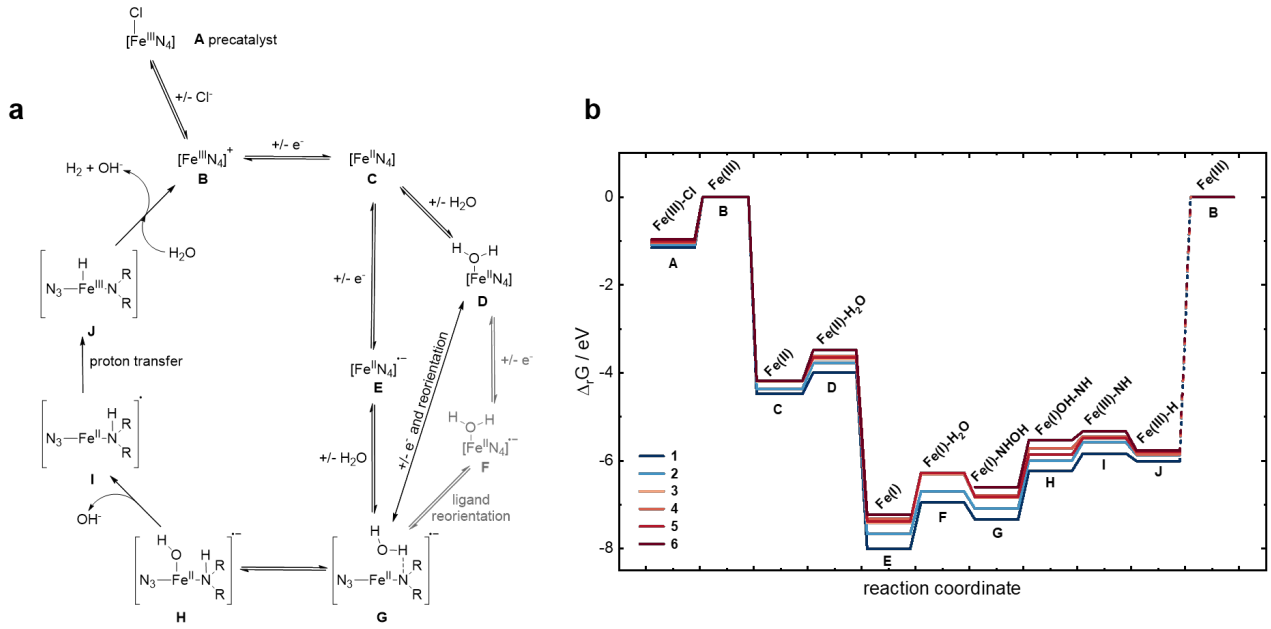

Figure 8: a) Proposed HER mechanism under alkaline conditions. b) Calculated Gibbs free enthalpies of HER intermediates relative to the Fe^{III} species. To improve legibility, the labels in (b) use the formal oxidation states, i.e. [**Fe(I)**P]$^{-}$ instead of [Fe(II)P$^{\bullet}$]$^{-}$.

the reduction step is associated with the onset of the HER.[16a,16c,37] Figures S12 and S13 show that properties of the iron atom extracted from OLYP calculations, such as the charge, the Mulliken spin population as a measure of unpaired electrons, and the isomer shift of both Fe^{II} and $[Fe^{II}(P^{\bullet})]^{-}$ again correlate poorly with the TOF. We note that the *changes* in these properties between Fe^{II} and $[Fe^{II}(P^{\bullet})]^{-}$ (see Figure S14) show clearer correlations with the TOF, in particular the isomer shift as a measure of electron density (see also Figure 7c). The less electron density at the iron nucleus is shifted during the Fe^{II} to $[Fe^{II}(P^{\bullet})]^{-}$ transition, the more active the complex. This indicates an involvement of the porphyrin ring in the rate-determining step. We note that complex **6,** which shows destabilized Fe^{II} in organic solvent, achieves higher HER activity in aqueous conditions compared to complexes with stable Fe^{II}.

Considering previous suggestions that the nitrogen ligand atoms can be involved in the reaction mechanism as internal bases,[38] this possibility was investigated more closely by us. Experimentally, the involvement of the N atoms is indicated by observations made in organic electrolyte. The highly instable Fe^{II} species of **6** in DCM results in the highest TOF of **6** in 0.1 M KOH. Due to the absence of other reactants in the inert organic electrolyte, the porphyrin decomposes. In contrast to this, Fe^{II} and even $[Fe^{II}(P^{\bullet})]^{-}$ species are very stable in case of **1** and **2**. Here, the reduced species are stabilized by the electron withdrawing groups. In 0.1 M KOH, **1** and **2** show low TOFs compared to the other iron porphyrins.

At the electronic structure level, this idea can be evaluated by correlating the number of unpaired electrons at the nitrogen ligand atoms with the TOF (see Figure 7d). To this end, the Mulliken spin population was extracted from OLYP single point calculations for the species Fe^{II} (**C**) and $[Fe^{II}(P^{\bullet})]^{-}$ (**E**, denoted as Fe(I) in Figure 8b and in the SI), and summed for all four nitrogen atoms. The sum was used because the differences between the substituted complexes are very small; we emphasize here that this measure should only be understood as an indicator and should not be used as a quantitative predictor. Similar to that, the predicted charge on the nitrogen atoms, as well as the spin population of the porphin plane seem to vaguely correlate with the TOF for both Fe^{II} and $[Fe^{II}(P^{\bullet})]^{-}$ (see Figure S12-S13). Even though the variation across the substituents is again very small, we suggest that the anion radical character is important for the HER activity, and furthermore that nitrogen is involved in the rate determining step in alkaline solution.

With this hypothesis in hand, we propose a new mechanistic proposal for adsorbed iron porphyrin complexes in aqueous electrolyte. As a first step, the role of water in the catalytic cycle is further investigated, namely by coordination to Fe^{II} or Fe^{I}, forming **D** and **F**, and further reaction via a transition state where OH is coordinated to Fe and H binds to one of the four nitrogen atoms, using the formal oxidation state notation Fe^{I}OH-NH (**H**) (see Figure 8, Figure S10). Geometries of these intermediates are exemplarily shown for **3** in Figure S9. Surprisingly, the coordination of water to Fe^{II} (**D**) and Fe^{I} (**F**) is disfavored by 0.5 - 0.7 eV and 1.0 - 1.1 eV, respectively. Additionally, the coordination of water to Fe^{I} (**F**) only resulted in stable geometries for complexes **1**, **2**, **3**, and **5**. These structures have a total spin S_{total} = $^{3}/_{2}$, i.e. a similar electronic configuration as for Fe^{I} (**E**, namely $[Fe^{II}(P^{\bullet})]^{-}$), but with a parallel alignment of the unpaired electrons on the porphin plane and the iron ion. We observed that geometry optimizations for this and other spin states repeatedly resulted in the coordination of H_2O towards one of the N atoms. Therefore, such a geometry, labeled Fe^{I}-NHOH (**G**), was added to the systematic study. The energetic cost for the coordination of water at a porphyrin nitrogen atom (**E**→**G**) was found to be only 0.5 - 0.7 eV and the electronic configuration matches that of $[Fe^{II}(P^{\bullet})]^{-}$, i.e. antiparallel alignment of spins on the iron ion and the porphyrin plane.

For the intermediate Fe^{I}OH-NH (**H**), two energetically close-lying spin states were found: doublet and sextet. After consideration of the entropy contribution to the Gibbs free enthalpies, S_{total} = $^{5}/_{2}$ was found to be more stable by 0.1 - 0.2 eV. The only exceptions are complex **6**, where only S_{total} = $^{5}/_{2}$ could be converged, and

complex **3**, for which a different, energetically unfavored electron configuration is found for $S_{total} = {}^5/_2$ (see SI Table S2-S3).
Even though the identification of the rate determining step within this mechanism by computational means is beyond the scope of this work, some estimates can be made: the highest thermodynamic obstacle for the reaction is the second reduction step (**C**→**E**, 3.0 - 3.4 eV), and the second largest is the O-H bond breaking step (**G**→**H**, 0.9 - 1.1 eV).
The reduction step from Fe^{II} (**C**) to Fe^{I} (**E**) by itself does not explain a possible involvement of porphinic nitrogen in the rate determining step. Relaxed surface scans for the O-H bond breaking process from Fe-NHOH (**G**) to Fe^{I}OH-NH (**H**; scan with $S_{total} = {}^1/_2$) do not show a transition state (see Figure S15). Capturing the spin state change for this reaction from the S_{total} = 1/2 species to the S_{total} = 5/2 product would require a scan with $S_{total} = {}^5/_2$. Since the method we chose for the relaxed surface scan does not capture the stabilizing entropic contributions for the high spin species, a complete comparison is outside the scope of this work. Consequently, this reaction step cannot be excluded as the rate determining step *per se*, but would require a barrier exceeding the Gibbs free enthalpy of 3.0 – 3.4 eV associated with the second reduction step. From the exemplary surface scans for H migration from Fe^{III}-NH (**I**) to Fe^{III}H (**J**), a reaction barrier of < 0.3 eV was estimated (see Figure S16), excluding this reaction step to be rate determining.
The barriers for OH^- abstraction from Fe^{I}OH-NH (**I**) and the reaction of Fe^{III}-H (**J**) to Fe^{III} (**B**) forming H_2 cannot be estimated via relaxed surface scans. However, these reaction steps do not require the involvement of N and thus do not fit with the reaction model derived above.
Another plausible rate determining step might be - after the first reduction step - a combined second reduction and water migration step from Fe^{II}-H_2O (**D**) to Fe(I)-NHOH (**G**). If the applied potential is sufficiently high for the coordination of water, forming **D**, the coordinated water is destabilized upon further reduction, forming the instable species **F**. The water molecule may therefore migrate to a porphinic nitrogen atom (**F** to **G**). This reaction may occur concertedly from **D** to **G**. Either would explain nitrogen involvement in the rate determining step. The Gibbs free enthalpies of the differently substituted complexes correlate remarkably well for this reaction step (Fe^{II}-H_2O + e^- → Fe^{I}-NHOH; **D** to **G**), R^2 = 0.9026 for TOF at 0.8 V and R^2 = 0.9136 for TOF at 0.7 V (see Figure S11f). Consequently, we propose the second reduction combined with water migration as the rate determining step. Further experiments will be required to verify this statement and to fully elucidate the HER mechanism on these model systems.

Conclusion

The influence of substituents in iron porphyrin complexes on the electrochemical characteristics, the interaction with a support, and the hydrogen evolution reaction was investigated by a combination of theory and experiment. The redox potentials determined in DCM/TBAP and in alkaline media correlate well with the electronic energy differences obtained from DFT calculations for the differently substituted porphyrin complexes. The partial density of states related to iron with and without support are similar and compare well with NRV spectra predicted for the isolated complexes. These findings show that the support has a limited or no effect on the pDOS. However, it is found that the choice of substituent alters the utilization: electron poor porphyrins connect better to the carbon black support, resulting in a higher utilization.
Correlating the substituent properties with the observed catalytic activity, we find that an increase in the electron donating power is associated with a decrease in the Fe^{II}/Fe^{III} redox potential and an increase of the TOF. DFT calculations show that the formal Fe(I) state is better described as an Fe(II) ion with a porphyrin radical ligand $[Fe^{II}(P^{\bullet})]^-$ with the unpaired electrons aligned antiparallel to those of the iron ion. Porphyrins that promote a shift of electron density in this reduced state towards the ligand π-system are more active in the HER. We connected experimental information with the predicted properties of plausible catalytic intermediates and suggest that one of the porphinic nitrogen atoms acts as an internal base towards a water molecule. This interaction facilitates an O-H bond breaking step of a water molecule in alkaline conditions, thus enabling higher TOF values.
Our results provide insights on the support effects of carbon supported porphyrin systems and thereby help to close the gap between homogeneous and heterogeneous catalysis. Our findings on the reaction mechanism are furthermore relevant in the context of MN_4 moieties integrated in amorphous carbon frameworks, where they might aid in the knowledge-based design of MNC catalysts as promising materials in PEC.

Experimental Section

Materials: All reagents are commercially available and were used without further purification. The iron porphyrins (>95 %) were purchased from Porphyrin-Laboratories GmbH, 5 wt% Nafion solution NS-5 from Quintech, BLACK PEARLS 2000 from CABOT and 0.25 mm thick Indium foil (99.99 % metal basis) from AlfaAesar. All other chemicals were obtained from Carl Roth.

Catalyst preparation: The iron porphyrin (0.23 mmol) was dissolved in 15 ml dichloromethane and treated in an ultrasonic bath for 5 min before BlackPearls2000 (100 mg, 1635 m^2g^{-1}) was added. Under ultrasonic treatment the solvent was allowed to evaporate completely. The drying process was completed by an overnight treatment at 80 °C in a drying oven. Finally, the obtained powder was homogenized in a mortar.

Electrochemistry: For electrochemical investigations a Princeton Applied Research set up was used, consisting of a PARSTAT 3000A DX, a 636 A rotator and a ring disk electrode with a glassy carbon disk electrode (d_{disk} = 5.5 mm, A_{disk} = 0.2376 cm^2). The potentials were referenced versus an Ag | AgCl | 3 M NaCl electrode in acid electrolyte and a Hg | HgO | 1 M NaOH electrode in alkaline electrolyte. Both types of reference electrodes were purchased from ALS via C3 Analytics. The reference electrodes were calibrated every day vs. a reversible hydrogen electrode from Gaskatel. As counter electrode glassy carbon rods purchased from HTW-Germany were used. For measurements in dichloromethane an Ag | $AgNO_3$ reference electrode from ALS was used and calibrated after every set of measurements in the same electrolyte mixture against ferrocene as an internal standard. The counter electrode was a platinum wire.

Measurements in organic electrolyte were conducted by producing a solution of 1 mM porphyrin and 0.1 M of tetrabutylammoium perchlorate (TBAP) as conducting agent in dichloromethane. The measurements were performed under constant saturation with N_2 in a custom made 5 necked cell with a filling capacity of 4 to 10 mL. An initial survey measurement was performed to determine the anodic and cathodic decomposition potentials. Then the vortex potentials for CVs were set below the decomposition

potentials and one CV was measured at 100 mV s^{-1} and 10 mV s^{-1} each. Afterwards ferrocene was added as internal standard to calibrate the reference electrode.

0.1 M H_2SO_4 aqueous electrolyte was prepared from concentrated (>98 %) acid by dilution with ultra-pure water with a resistance of 18.2 Ω or higher. 0.1 KOH electrolyte was prepared by dissolving KOH pellets in ultra-pure water. The catalyst layer was deposited on a freshly polished glassy carbon disk electrode by deploying an ink. For the ink preparation 5 mg of catalyst are dispersed in 142 µL water and then subsequently 25 µL 5 wt% Nafion solution, 83.3 µL and 125 µL 0.1 M H_2SO_4 were added. For ideal dispersion the mixture is placed alternately into an ice cooled ultrasonic bath (USB) and on an orbital shaker. After 45, 15 and 1 min in the USB the ink is placed for 1 min in the shaker. 9 µL of the freshly prepared ink was then drop casted on the glassy carbon disk electrode and left to dry to obtain a loading of 0.51 mg cm^{-2}. Prior to drop-casting, the GC disk was polished. Therefore, a 0.05 µm alumina polish and a MasterTex polishing pad were used. Close before complete drying of the catalyst layer, the process is quenched by a drop of electrolyte, to reach a homogeneous catalyst layer. The electrode was then mounted on the rotator and positioned in the electrolyte. A beaker like cell was used filled with 50 mL N_2 saturated premixed electrolyte. The measurements were performed under constant saturation of the electrolyte with N_2. For conditioning of the catalyst layer a set of cyclic voltammetry measurements were performed between 0 and 1.1 V vs RHE, namely 20 cycles at 300 mV s^{-1}, and one at 100 mV s^{-1}, 50 mV s^{-1} and 10 mV s^{-1} each. The hydrogen evolution reaction was measured in a potential range from 0.1 V to -1 V vs RHE. Three cycles were performed, but only the second one was evaluated for interpretation of the activity. The first cycle serves as an activation and the third is used to check the reproducibility of the evaluated cycle. Both are not further discussed here. In general, the activity in the third cycle was slightly lower than in the second cycle. With a overpotential drops of less than 30 mV at 10 mA cm^{-2}, we consider the electrode layer sufficiently stable.

Nuclear Resonance Vibration Spectroscopy: (alternative nomenclature: nuclear resonance inelastic X-ray scattering NRIXS or nuclear inelastic scattering NIS) was performed at the P01 High Resolution Dynamics beamline at PETRA III (Deutsches Elektronen-Synchrotron, DESY) during the beamtime I-20200863. The synchrotron operated with a 40 bunches filling mode and a photon energy of 14.4 keV (^{57}Fe resonance) is selected at the P01 beamline. The energy is tunable in the meV range by a high resolution monochromator. Thin packages of 1 – 3 mg sample powder were prepared by pressing in the sample between two layers of Mylar aluminium foil. These packages were placed on a copper sample holder in a closed cycle cryostat (6-800 K). The NRVS scans were performed at a temperature between 17 and 28 K. The exact measurement temperature was determined from the original measured data and differed due to variation in thermal contacting. Scattered photons were detected by an avalanche photodiode (APD). From the NRVS scans the partial density of states (pDOS) related to iron was calculated.[27a,39]

X-ray photoelectron spectroscopy: XPS samples were prepared by pressing a homogenized powder onto an 8 by 8 mm piece of indium foil, which is then mounted on a stainless-steel sample holder. Afterwards, the sample was introduced into ultra-high vacuum (UHV) at the Darmstadt Integrated System for Fundamental research (DAISY-FUN).[40] It is equipped with a PHOIBOS 150 hemispherical analyser, CEM 9 Channeltron analyser and a XR50M x-ray source, all three from SPECS Surface Nano Analysis GmbH. The XPS measurements were performed at pressures below $1 \cdot 10^{-9}$ mbar with monochromatic excitation by Al Kα (1486.64 eV) radiation. The pass energy was set to 20 eV for the survey scans, to 20 eV for high resolution (HR) Fe 2p scans and to 10 eV for all other HR scans. The setup is calibrated using Cu 2p, Ag 3d and Au 4f core levels and valence band edges. The used evaluation software was Igor Pro. The obtained spectra were analysed with CasaXPS. The background in HR-XPS was determined as Shirley type, to accommodate for inelastic electron scattering. The signals were fitted with a Gaussian/Lorentzian (70/30) line shape model.

Computational Details: All calculations were carried out using version 4.2.1. of the ORCA suite of programs.[41] Geometry optimizations and subsequent frequency calculations were performed using the TPSS[42] density functional in unrestricted Kohn-Sham density functional theory and Ahlrichs' basis set def2-SVP[43] for the description of C and H atoms while def2-TZVP[43] was used for all other atoms, namely Fe, O and Cl. Split-RI-J approximation was employed using the def2/J basis set.[44] The convergence criteria for SCF and geometry optimisation were set to "tight" in ORCA nomenclature. The size of the radial grid and the angular grid was to 6.0. Dispersion correction by Grimme with Becke-Johnson damping (D3BJ) was employed[45] and water was used as an implicit solvent within the SMD model.[46] Single point calculations using the B3LYP[47] functional were performed on the optimized geometries for the prediction of Mössbauer parameters as previously described by the authors.[26] The electronic structures were evaluated from single point calculations with the identic settings as Mössbauer prediction calculation, but with the OLYP density functional[47b,48] and without dispersion correction. From the optimized geometries and frequency calculations Gibbs free enthalpies were obtained and corrected using the electronic energies obtained from the OLYP calculations. Reaction enthalpies were calculated for the following reactions:

Fe(III)-Cl → Fe(III) + Cl^-	I
Fe(III) + e^- → Fe(II)	II
Fe(II) + e^- → Fe(I)	III
Fe(I) + H_2O → Fe(III)-H + OH^-	IV
Fe(II) + H_2O → Fe(II)-H_2O	V
Fe(I) + H_2O → Fe(I)-H_2O	VI
Fe(I) + H_2O → Fe(I)-NHOH	VII
Fe(I)-NHOH → Fe(I)OH-NH	VIII
Fe(I)OH-NH → Fe(III)-NH + OH^-	IX
Fe(III)-NH → Fe(III)-H	X

The corrected Gibbs free enthalpies of formation of small molecules, namely Cl^-, H_2O and OH^- were computed using the same settings and are given in Table S10 where required for the reaction. Relaxed surface scans were performed for reaction VIII and X fixing the bond length of O-H and Fe-H, respectively, starting from the optimized geometry of the reactant. For each step of the relaxed surface scan, the bond length was fixed for each step (0.98 to 2.50 Å, 20 steps for VIII and 2.10 to 1.45 Å, 45 steps for X) followed by a geometry optimization of the rest of the molecule with the same settings as mentioned beforehand.

For NRVS, optimized geometries were reoptimized using the B3LYP[47] density functional and RIJCOSX[49] approximation with otherwise identical settings. A frequency calculation was performed on these structures with the same approach. The spectra were extracted from the Hessian file using the orca_mapspc subprogram and the NRVS keyword and a Gaussian band broadening of 15 cm^{-1} was chosen. Visualisations were carried out in Chimera 1.13.1 and Origin 2020b.

Acknowledgements

Financial support from Deutsche Forschungsgemeinschaft (DFG PAK981 with KR3980/8-1 and JA 859/34-1) is gratefully acknowledged. CG acknowledges support from Merck'sche Gesellschaft für Kunst und Wissenschaft e.V. We gratefully acknowledge the beamtime I-20200863 at the P01 beamline at

Petra III, DESY, Hamburg, Germany. CG and VK acknowledge computing time for this research project on the HHLR Lichtenberg high-performance computer at TU Darmstadt.

Keywords: Hydrogen • Electrochemistry • Heterogeneous catalysis • Density functional theory • molecular electrochemistry • renewable resources

[1] bp Statistical Review of World Energy 2021.

[2] I. Roger, M. A. Shipman, M. D. Symes, Nat Rev Chem 2017, 1, 928.

[3] M. G. Walter, E. L. Warren, J. R. McKone, S. W. Boettcher, Q. Mi, E. A. Santori, N. S. Lewis, *Chem. Rev.* **2010**, *110*, 6446–6473.

[4] C. C. L. McCrory, S. Jung, I. M. Ferrer, S. M. Chatman, J. C. Peters, T. F. Jaramillo, *J. Am. Chem. Soc.* **2015**, *137*, 4347–4357.

[5] a) A. Shahraei, I. Martinaiou, K. A. Creutz, M. Kübler, N. Weidler, S. T. Ranecky, W. D. Z. Wallace, M. A. Nowroozi, O. Clemens, R. W. Stark, U. I. Kramm, *Chem. Eur. J.* **2018**, *24*, 12480–12484; b) A. Shahraei, A. Moradabadi, I. Martinaiou, S. Lauterbach, S. Klemenz, S. Dolique, H.-J. Kleebe, P. Kaghazchi, U. I. Kramm, ACS applied materials & interfaces **2017**, *9*, 25184–25193; c) J. Wang, J. Kim, S. Choi, H. Wang, J. Lim, Small Methods **2020**, *4*, 2000621;

[6] a) G. Wu, K. L. More, C. M. Johnston, P. Zelenay, Science 2011, 332, 443–447; b) D. Banham, T. Kishimoto, Y. Zhou, T. Sato, K. Bai, J.-I. Ozaki, Y. Imashiro, S. Ye, *Sci. Adv.* **2018**, *4*, eaar7180; c) L. Ni, C. Gallenkamp, S. Paul, M. Kübler, P. Theis, S. Chabbra, K. Hofmann, E. Bill, A. Schnegg, B. Albert, V. Krewald, U. I. Kramm, *Adv. Energy Sustain. Res.* **2021**, *2*, 2000064; d) L. Ni, C. Gallenkamp, S. Wagner, E. Bill, V. Krewald, U. I. Kramm, ChemRxiv 2022, doi: 10.26434/chemrxiv-2022-td60c; e) U. I. Kramm, J. Herranz, N. Larouche, T. M. Arruda, M. Lefèvre, F. Jaouen, P. Bogdanoff, S. Fiechter, I. Abs-Wurmbach, S. Mukerjee, J.-P. Dodelet, *Phys. Chem. Chem. Phys.* **2012**, *14*, 11673–11688; f) E. Proietti, F. Jaouen, M. Lefèvre, N. Larouche, J. Tian, J. Herranz, J.-P. Dodelet, *Nat. Commun.* **2011**, 2, 1–9;

[7] a) A. Bagger, W. Ju, A. S. Varela, P. Strasser, J. Rossmeisl, *Catalysis Today* **2017**, *288*, 74–78; b) T. N. Huan, N. Ranjbar, G. Rousse, M. Sougrati, A. Zitolo, V. Mougel, F. Jaouen, M. Fontecave, *ACS Catalysis* **2017**, *7*, 1520–1525; c) S. Paul, Y.-L. Kao, L. Ni, R. Ehnert, I. Herrmann-Geppert, R. van de Krol, R. W. Stark, W. Jaegermann, U. I. Kramm, P. Bogdanoff, *ACS Catalysis* **2021**, **11**, 5850–5864;

[8] a) M. J. M. Nesset, N. V. Shokhirev, P. D. Enemark, S. E. Jacobson, F. A. Walker, *Inorg. Chem.* **1996**, *35*, 5188–5200; b) I. Martinaiou, T. Wolker, A. Shahraei, G.-R. Zhang, A. Janßen, S. Wagner, N. Weidler, R. W. Stark, B. J.M. Etzold, U. I. Kramm, *J. Power Sources* **2018**, *375*, 222–232;

[9] a) S. Wagner, H. Auerbach, C. E. Tait, I. Martinaiou, S. C. N. Kumar, C. Kübel, I. Sergeev, H. ‐ C. Wille, J. Behrends, J. A. Wolny, V. Schünemann, U. I. Kramm, *Angew. Chem. Int. Ed.* **2019**, *58*, 10486‐10492; b) T. Mineva, I. Matanovic, P. Atanassov, M.-T. Sougrati, L. Stievano, M. Clémancey, A. Kochem, J.-M. Latour, F. Jaouen, *ACS Catalysis* **2019**, *9*, 9359–9371; c) J. L. Kneebone, S. L. Daifuku, J. A. Kehl, G. Wu, H. T. Chung, M. Y. Hu, E. E. Alp, K. L. More, P. Zelenay, E. F. Holby, M. L. Neidig, *J. Phys. Chem. C* **2017**, *121*, 16283–16290;

[10] a) J. Li, M. T. Sougrati, A. Zitolo, J. M. Ablett, I. C. Oğuz, T. Mineva, I. Matanovic, P. Atanassov, Y. Huang, I. Zenyuk, A. Di Cicco, K. Kumar, L. Dubau, F. Maillard, G. Dražić, F. Jaouen, *Nat. Catal.* **2021**, *4*, 10–19; b) X. Li, C.-S. Cao, S.-F. Hung, Y.-R. Lu, W. Cai, A. I. Rykov, S. Miao, S. Xi, H. Yang, Z. Hu, J. Wang, J. Zhao, E. E. Alp, W. Xu, T.-S. Chan, H. Chen, Q. Xiong, H. Xiao, Y. Huang, J. Li, T. Zhang, B. Liu, *Chem* **2020**, *6*, 3440–3454; c) A. Zitolo, V. Goellner, V. Armel, M.-T. Sougrati, T. Mineva, L. Stievano, E. Fonda, F. Jaouen, *Nat. Mater.* **2015**, *14*, 937–942;

[11] F. Luo, A. Roy, L. Silvioli, D. A. Cullen, A. Zitolo, M. T. Sougrati, I. C. Oguz, T. Mineva, D. Teschner, S. Wagner, J. Wen, F. Dionigi, U. I. Kramm, J. Rossmeisl, F. Jaouen, P. Strasser, *Nat. Mater.* **2020**, *19*, 1215–1223.

[12] a) U. I. Kramm, M. Lefèvre, N. Larouche, D. Schmeisser, J.-P. Dodelet, *J. Am. Chem. Soc.* **2014**, *136*, 978–985; b) Q. Lin, X. Bu, A. Kong, C. Mao, F. Bu, P. Feng, *Adv. Mater.* **2015**, *27*, 3431–3436; c) S. Brüller, H.-W. Liang, U. I. Kramm, J. W. Krumpfer, X. Feng, K. Müllen, *J. Mater. Chem. A* **2015**, *3*, 23799–23808;

[13] a) C. Gueutin, D. Lexa, M. Momenteau, J. M. Saveant, F. Xu, *Inorg. Chem.* **1986**, *25*, 4294–4307; b) J. Masa, K. Ozoemena, W. Schuhmann, J. H. Zagal, *J. Porphyrins Phthalocyanines* **2012**, *16*, 761–784; c) W. A. Lee, T. S. Calderwood, T. C. Bruice, *Proc. Nat. Acad. Sci.* **1985**, *82*, 4301–4305;

[14] E. Tabor, J. Połtowicz, K. Pamin, S. Basąg, W. Kubiak, *Polyhedron* **2016**, *119*, 342–349.

[15] a) Y. Jiao, Y. Zheng, K. Davey, S.-Z. Qiao, *Nat. Energy* **2016**, *1*, 43; b) J. H. Zagal, S. Griveau, K. I. Ozoemena, T. Nyokong, F. Bedioui, *Journal of nanoscience and nanotechnology* **2009**, *9*, 2201–2214;

[16] a) D. J. Graham, D. G. Nocera, *Organometallics* **2014**, *33*, 4994–5001; b) B. B. Beyene, S. B. Mane, C.-H. Hung, *Chem. Commun.* **2015**, *51*, 15067–15070; c) B. B. Beyene, C.-H. Hung, *Coord. Chem. Rev.* **2020**, *410*, 213234; d) Y. Han, H. Fang, H. Jing, H. Sun, H. Lei, W. Lai, R. Cao, *Angew. Chem. Int. Ed.* **2016**, *55*, 5457–5462; e) X. Hu, B. S. Brunschwig, J. C. Peters, *J. Am. Chem. Soc.* **2007**, *129*, 8988–8998; f) C. H. Lee, D. K. Dogutan, D. G. Nocera, *J. Am. Chem. Soc.* **2011**, *133*, 8775–8777; g) Y.-Q. Zhong, M. S. Hossain, Y. Chen, Q.-H. Fan, S.-Z. Zhan, H.-Y. Liu, *Transit. Met. Chem.* **2019**, *44*, 399–406; h) B. Mondal, K. Sengupta, A. Rana, A. Mahammed, M. Botoshansky, S. G. Dey, Z. Gross, A. Dey, *Inorg. Chem.* **2013**, *52*, 3381–3387;

[17] a) N. Queyriaux, N. Kaeffer, A. Morozan, M. Chavarot-Kerlidou, V. Artero, *J. Photochem. Photobio. C.* **2015**, *25*, 90–105; b) R. M. Kellett, T. G. Spiro, *Inorg. Chem.* **1985**, *24*, 2373–2377; c) T. Abe, F. Taguchi, H. Imaya, F. Zhao, J. Zhang, M. Kaneko, *Polymers for Advanced Technologies* **1998**, *9*, 559–562;

[18] a) K. M. Kadish, K. M. Smith, R. Guilard, The porphyrin handbook; Academic Press, San Diego, Calif, London, 2000-2003; b) K. M. Kadish, K. M. Smith, R. Guilard, The porphyrin handbook; Academic Press, San Diego, Calif, London, 2000-2003;

[19] L. A. Bottomley, K. M. Kadish, *Inorg. Chem.* **1981**, *20*, 1348–1357.

[20] C. Swistak, X. H. Mu, K. M. Kadish, *Inorg. Chem.* **1987**, *26*, 4360–4366.

[21] a) C. K. Jorgensen, Oxidation Numbers and Oxidation States; Springer Berlin / Heidelberg, Berlin, Heidelberg, 1969; b) P. Chaudhuri, C. N. Verani, E. Bill, E. Bothe, T. Weyhermüller, K. Wieghardt, *J. Am. Chem. Soc.* **2001**, *123*, 2213–2223;

[22] K. Yamaguchi, I. Morishima, *Inorg. Chem.* **1992**, *31*, 3216–3222.

[23] a) É. Anxolabéhère, G. Chottard, D. Lexa, *New J. Chem.* **1994**, *18*, 889–899; b) C. Römelt, S. Ye, E. Bill, T. Weyhermüller, M. van Gastel, F. Neese, *Inorg. Chem.* **2018**, *57*, 2141–2148; c) G. N. Sinyakov, A. M. Shulga, *J. Mol. Struc.* **1993**, *295*, 1–14;

[24] a) J. Ho, *Phys. Chem. Chem. Phys.* **2015**, *17*, 2859–2868; b) V. Krewald, D. A. Pantazis, *Dalton Trans.* **2016**, *45*, 18900–18908; c) V. Krewald, F. Neese, D. A. Pantazis, *Phys. Chem. Chem. Phys.* **2016**, *18*, 10739–10750.

[25] P. Gütlich, Mössbauer Spectroscopy and Transition Metal Chemistry; Springer Berlin / Heidelberg, Berlin, Heidelberg, 1978.

[26] C. Gallenkamp, U. I. Kramm, J. Proppe, V. Krewald, *Int. J. Quantum Chem.* **2020**, *63*, e26394.

[27] a) W. R. Scheidt, J. Li, J. T. Sage, *Chem. Rev.* **2017**, *117*, 12532–12563; b) B. Moeser, A. Janoschka, J. A. Wolny, H. Paulsen, I. Filippov, R. E. Berry, H. Zhang, A. I. Chumakov, F. A. Walker, V. Schünemann, *J. Am. Chem. Soc.* **2012**, *134*, 4216–4228; c) A. Barabanschikov, A. Demidov, M. Kubo, P. M. Champion, J. T. Sage, J. Zhao, W. Sturhahn, E. E. Alp, *J. Chem. Phys.* **2011**, *135*, 15101; d) S. Wagner, H. Auerbach, C. E. Tait, I. Martinaiou, S. C. N. Kumar, C. Kübel, I. Sergeev, H.-C. Wille, J. Behrends, J. A. Wolny, V. Schünemann, U. I. Kramm, *Angew. Chem.* **2019**, *131*, 10596–10602.

[28] a) T. Ohta, J.-G. Liu, M. Saito, Y. Kobayashi, Y. Yoda, M. Seto, Y. Naruta, *J. Phys. Chem. B* **2012**, *116*, 13831–13838; b) C. Hu, A. Barabanschikov, M. K. Ellison, J. Zhao, E. E. Alp, W. Sturhahn, M. Z. Zgierski, J. T. Sage, W. R. Scheidt, *Inorg. Chem.* **2012**, *51*, 1359–1370; c) B. M. Leu, M. Z. Zgierski, G. R. A. Wyllie, W. R. Scheidt, W. Sturhahn, E. E. Alp, S. M. Durbin, J. T. Sage, *J. Am. Chem. Soc.* **2004**, *126*, 4211–4227;

[29] N. J. Silvernail, A. Barabanschikov, J. W. Pavlik, B. C. Noll, J. Zhao, E. E. Alp, W. Sturhahn, J. T. Sage, W. R. Scheidt, *J. Am. Chem. Soc.* **2007**, *129*, 2200–2201.

[30] F. Paulat, V. K. K. Praneeth, C. Näther, N. Lehnert, *Inorg. Chem.* **2006**, *45*, 2835–2856.
[31] a) D. H. Karweik, N. Winograd, *Inorg. Chem.* **1976**, *15*, 2336–2342; b) Qi-Zhi Ren, Jin-Wang Huang, Zhi-Ang Zhu, Liang-Nian Ji, Yun-Ti Chen, *Journal of Porphyrins and Phthalocyanines* **2001**, *5*, 449–455; c) Z. Wang, K. Qian, M. A. Öner, P. S. Deimel, Y. Wang, S. Zhang, X. Zhang, V. Gupta, J. Li, H.-J. Gao, D. A. Duncan, J. V. Barth, X. Lin, F. Allegretti, S. Du, C.-A. Palma, *ACS Applied Nano Materials* **2020**, *3*, 11752–11759;
[32] a) Antoine Maurin, Marc Robert, *Chem. Commun.* **2016**, *52*, 12084–12087; b) J. H. Zagal, S. Griveau, J. F. Silva, T. Nyokong, F. Bedioui, *Coord. Chem. Rev.* **2010**, *254*, 2755–2791;
[33] a) D. Huang, J. Lu, S. Li, Y. Luo, C. Zhao, B. Hu, M. Wang, Y. Shen, *Langmuir* **2014**, *30*, 6990–6998; b) J. Ma, L. Liu, Q. Chen, M. Yang, D. Wang, Z. Tong, Z. Chen, *Appl. Surf. Sci.* **2017**, *399*, 535–541; c) H. Li, X. Li, H. Lei, G. Zhou, W. Zhang, R. Cao, *ChemSusChem* **2019**, *12*, 801–806; d) C. Canales, A. F. Olea, L. Gidi, R. Arce, G. Ramírez, *Electrochim. Acta* **2017**, *258*, 850–857; e) C. Canales, F. Varas-Concha, T. E. Mallouk, G. Ramírez, *Appl. Cat. B* **2016**, *188*, 169–176;
[34] a) B. B. Beyene, A. W. Yibeltal, C. H. Hung, *Inorg. Chim. Acta* **2020**, *513*, 119929; b) Belete B. Beyene, Sandeep B. Mane, Chen-Hsiung Hung, *J. Electrochem. Soc.* **2018**, *165*, H481;
[35] I. Bhugun, D. Lexa, J.-M. Savéant, *J. Am. Chem. Soc.* **1996**, *118*, 3982–3983.
[36] E. S. Wiedner, M. B. Chambers, C. L. Pitman, R. M. Bullock, A. J. M. Miller, A. M. Appel, *Chem. Rev.* **2016**, *116*, 8655–8692.
[37] D. J. Graham, D. K. Dogutan, Matthias Schwalbe, D. G. Nocera, *Chem. Commun.* **2012**, *48*, 4175–4177.
[38] a) L. Cao, Q. Luo, W. Liu, Y. Lin, X. Liu, Y. Cao, W. Zhang, Y. Wu, J. Yang, T. Yao, S. Wei, *Nat. Catal.* **2019**, *2*, 134–141; b) A. A. Tanaka, C. Fierro, D. A. Scherson, E. Yeager, *Materials Chemistry and Physics* **1989**, *22*, 431–456;
[39] A. Chumakov, R. Rüffer, *Hyperfine Interactions* **1998**, *113*, 59–79.
[40] W. Jaegermann, B. Kaiser, J. Ziegler, J. Klett in Photoelectrochemical solar fuel production. From basic principles to advanced devices / Sixto Giménez, Juan Bisquert, editors; (Eds. S. Giménez, J. Bisquert), Springer, Switzerland, 2016, pp. 199–280.
[41] Frank Neese, *WIRES* **2012**, *2*, 73–78.
[42] J. Tao, J. P. Perdew, V. N. Staroverov, G. E. Scuseria, *Phys. Rev. Lett.* **2003**, *91*, 146401.
[43] Florian Weigend, Reinhart Ahlrichs, *Phys. Chem. Chem. Phys.* **2005**, *7*, 3297–3305.
[44] Florian Weigend, *Phys. Chem. Chem. Phys.* **2006**, *8*, 1057–1065.
[45] a) S. Grimme, J. Antony, S. Ehrlich, H. Krieg, *J. Chem. Phys.* **2010**, *132*, 154104; b) S. Grimme, S. Ehrlich, L. Goerigk, *J. Comp. Chem.* **2011**, *32*, 1456–1465;
[46] A. V. Marenich, C. J. Cramer, D. G. Truhlar, *J. Phys. Chem. B* **2009**, *113*, 6378–6396.
[47] a) A. D. Becke, *J. Chem. Phys.* 1993, 98, 5648; b) C. Lee, W. Yang, R. G. Parr, *Phys. Rev. B* **1988**, *37*, 785;
[48] N. C. Handy, A. J. Cohen, *Mol. Phys.* **2001**, *99*, 403–412.
[49] F. Neese, F. Wennmohs, A. Hansen, U. Becker, *Chem. Phys.* **2009**, *356*, 98–109.